ARTICLE

Magnetocaloric Effect in Mn-rich Heusler derived Alloys for Room Temperature Application

Received 00th January 20xx,
Accepted 00th January 20xx

DOI: 10.1039/x0xx00000x

Nishant Tiwari[a$], Subhendu Mishra[b$], Suman Sarkar[c], Saikat Talapatra[d], Mithun Palit[e], Manas Paliwal*[a], Abhishek K. Singh*[b], and Chandra Sekhar Tiwary*[a]

Magnetic refrigeration-based technologies rely on magnetocaloric properties of materials, and are crucial for improving energy efficiency as well as support clean environments. However, materials possessing significant magnetocaloric properties that can be used for room temperature-based applications are still lacking. Heusler alloys (such as Mn-Ni-Ga) shows giant magnetocaloric effects, which can be further improved by tuning its composition. Here, we have optimized the ratio of Ni and Ga to achieve unique magnetocaloric properties. The alloy demonstrates a substantial magnetocaloric effect, attributed to its narrow temperature range for both structural and magnetic phase transitions (near room temperature with minimal hysteresis). The structural phase changes are also observed through high-resolution transmission electron microscopy. The optimum entropy changes, calculated from isothermal magnetization curves (4 Tesla magnetic field) are found to be 24.50 J/kg-K which is higher as compared to state-of-art alloys. Experimental demonstration of magnetocaloric effect (refrigeration cycle) is also shown with the help of thermal imaging camera. First principle calculations were also conducted to validate the experimental findings, specifically focusing on the compositional effects on the structural transitions and magnetic properties of the investigated MNG alloys.

Keywords: Magnetocaloric effect; Heusler alloy, magneto-structural transition; DFT, Microscopy

Introduction

Magnetic refrigeration, utilizing magnetocaloric effect (MCE), has the potential to significantly enhance the energy efficiency of refrigeration system with a sustainable approach. MCE is a property of magnetic materials that can be triggered by the application of an external magnetic field [1,2]. Similar to conventional refrigeration systems, a magnetic refrigerator utilizes magnetocaloric materials (MCMs) to absorb heat from a low-temperature source (cold exchanger) and release it to a higher-temperature environment (hot exchanger) [3]. A key challenge in magnetic refrigeration is finding materials with a strong magnetocaloric response that can be effectively used for room temperature cooling. While many materials exhibit large magnetocaloric responses, they often have other drawbacks that limit their practical application [4].

Rare earth metal example, Gadolinium (Gd) based alloys shows MCE properties value (total entropy change (ΔS_T)) 12 J/kg-K at 7 T (Tesla) field across the Curie temperature (T_C). Gd stands out among all the pure rare earth elements and has Tc which is nearby room temperature [5]. Apart from Gd based alloys, Eu based oxides and alloys also shows promising magnetocaloric properties at very small magnetic field which make them suitable form the perspective of practical application [6–8]. Later, giant magnetocaloric effect (GMCE) has been discovered due to magneto-structural phase transition and magneto-elastic transition occurs in $Gd_5Si_2Ge_2$ [9], Heusler alloys [10–12] and La-Fe-Si [13], Mn-Fe-P-As[14] respectively. In a magneto-structural transition the symmetry of the lattice structure changes across the magnetic transition, while in a magneto-elastic transition the symmetry of the lattice structure remains unchanged across the magnetic transition. In recent times, Heusler alloys have garnered significant interest from the scientific community due to their versatile properties, such as their ability to exhibit shape memory effects, MCE, and magnetoresistance [15]. Among the large family of Heusler alloys, Mn-Ni-Ga based alloy system attracted a lot of attention from scientific community due to the presence of GMCE [16]. The key factor enabling GMCE is the presence of a structural transformation from cubic austenite (high temperature phase) to martensitic (low temperature phase), coupled with a magnetic phase transition. The martensite phase can exhibit complex structures at low temperature, such as monoclinic, orthorhombic, and modulated tetragonal structures like 5M/10M/7M, or a non-modulated tetragonal structure. These structures vary based on the concentration of Gallium and specific processing conditions [17,18]. In Heusler alloys, it is interesting that a significant alteration in the magnetocaloric behaviour can occur with just a slight change in stoichiometry, atomic arrangement, symmetry, or processing techniques. Depending upon the stoichiometry, Mn-Ni-Ga based Heusler alloys can be characterized into two subgroups namely full Heusler alloy having 2:1:1 (Ni_2MnGa) stoichiometry and the other is half Heusler alloys have different stoichiometry. In Mn-Ni-Ga alloy system both structural phase transition (Martensite to Austenite) temperature (T_M) and magnetic phase transition (ferromagnetic to paramagnetic transition) temperature (T_C) strongly depend on

[a] *Department of Metallurgical and Materials Engineering, Indian Institute of Technology Kharagpur, West Bengal 721302, India*
[b] *Materials Research Centre, Indian Institute of Science, Bengaluru 560012, Karnataka, India*
[c] *Department of Materials Engineering, Indian Institute of Technology Jammu, Jammu 181221, India*
[d] *School of Physics and Applied Physics, Southern Illinois University, Carbondale, IL 62901, USA*
[e] *Powder Processing Group, Defence Metallurgical Research Laboratory, Kanchanbagh, Hyderabad 500058, India*

Supplementary Information available: SEM-EDS analysis of the alloys, Isothermal magnetization data, Comparative studies of thermal hysteresis data and Schematic of magnetic refrigeration cycle. See DOI: 10.1039/x0xx00000x

electronic configuration (e/a) ratio [19]. With a constant amount of Ni, an increase in Mn concentration will result in a higher transformation temperature. Similarly, keeping Ga constant, increasing the Ni content relative to Mn will raise the transformation temperature. Apart from varying stoichiometry, introducing another element like Cu and Fe in the Mn-Ni-Ga matrix can also help in tuning T_C and T_M [20]. In $Ni_2Mn_{1-x}M_xGa$ (M= Cu) replacing Mn with Cu leads in tuning of both transition temperatures (T_C, T_M) and increase the magnetocaloric response by ten times for X = 0.25 [21]. In case of Fe, substitution of 1 at. % of Fe for Ni tune both the transition temperature which affects the magnetocaloric properties [22].

In present study, we present our investigations on Mn-Ni-Ga system, with compositions featuring (unexplored) Mn-rich region and chosen using a CALPHAD-assisted thermodynamic database [23]. Samples were selected with a constant Mn content and varying Ni and Ga, as illustrated in **Figure 1(a)**, denoted as MNG-1 ($Mn_{70}Ni_{25}Ga_5$), MNG-2 ($Mn_{70}Ni_{13}Ga_{17}$), and MNG-3 ($Mn_{70}Ni_5Ga_{25}$). This approach allows for a systematic investigation of how the atomic concentrations of Ni and Ga influence the MCE. While Manganese (Mn) concentration in the investigated alloys varies slightly, within a range of ±2 wt. %, largely due to the oxidizing tendencies of Mn. This methodology enables fine-tuning of stoichiometric Heusler alloys in the Mn-rich region, which can help adjust different transition temperatures (T_M, T_C). The alloys were prepared using the induction melting technique, followed by homogenization at 1073 K and ice water quenching (Further detail are provided in the next section). The microstructures of the alloys were examined using high-resolution transmission electron microscopy (HR-TEM) equipped with energy-dispersive spectroscopy in scanning transmission electron microscopy (EDS-STEM), Scanning electron microscopy (SEM) and X-ray diffraction (XRD). Furthermore, magnetocaloric properties were analysed using magnetization versus temperature (M-T) and isothermal magnetization (M-H) curves. Thermal analysis using differential scanning calorimetry (DSC) was also conducted in the investigated alloys. Along with that, we have also analyzed the thermal fluctuations with and without the presence of magnetic fields with the help of a thermal imaging camera to validate magnetocaloric effect. To further verify our experimental findings, density functional theory (DFT) calculations were also performed to explore the relationship between measured and calculated T_C and T_M data of MNG-1 and MNG-2. DFT calculations were performed to simulate structural changes in the investigated alloys at different temperatures using *ab-initio* Molecular Dynamics (AIMD). The DFT studies indicated that the lattice parameter of the relaxed structure changes with temperature, confirming the structural transformation temperature. Additionally, T_C was also calculated considering the ferromagnetic ground state of the investigated alloys. The Density of States (DOS) calculations confirmed that the magnetic contribution mainly comes from Mn atoms, for the concentration studied. As the atomic positions changes with temperature which lead to change in magnetic moment, thus magnetic moment is calculated at each temperature. The magnetic moment starts decreasing at a certain point, indicating the ferromagnetic to paramagnetic transition and confirming the T_C value for MNG-1 and MNG-2.

Material Synthesis

Materials and Experimental Methods

Three 20-gram alloys with specified compositions **(as detailed in Table 1))** were melted by using high-purity (99.9%) Ni (nickel), Mn (manganese), and Ga (gallium) elements, through induction melting in an argon atmosphere. To account for the volatility of manganese, an excess of 1 atomic percent was deliberately added during melting. Subsequently, the samples were sealed under vacuum then filled with argon in quartz tubes to prevent oxidation, a step taken due to their high Mn content. They were annealed at 1073 K for 7 days followed by quenching in ice water.

The composition of the as-cast alloys was determined using PAN Analytics X-Ray fluorescence (XRF) instrument. The crystallographic information of homogenized samples is investigated using a Cu-K_α target in Bruker D8 advance diffractometer in the range of 2θ = 20˚-90˚. The prepared alloys were examined for their microstructure and compositions using a ZEISS GEMINI 600 field-emission scanning electron microscope (FE-SEM). This setup allows for both quantitative and qualitative analysis of the microstructural features developed in the samples. Structural characterization was carried out using a JEOL JEM 2100F high-resolution transmission electron microscope (HR-TEM) operated at 200 kV. Additionally, EDS-STEM (Energy Dispersive Spectroscopy-Scanning Transmission Electron Microscopy) was employed for elemental mapping. The preparation of thin lamellae for Transmission Electron Microscopy (TEM) is crucial, especially for brittle materials, where traditional mechanical thinning methods can introduce cracks or defects. The ion milling method provides a controlled way to achieve ultra-thin sections without excessive mechanical stress. In present work, lamella preparation is carried out using the ion milling method due to the brittleness of the sample. Initially, the sample is cut using a wire cutter, followed by mechanical polishing to reduce its thickness to 100 µm. A 3 mm diameter disc is then obtained using a disc punch. Next, the dimpling process is performed to further thin the centre of the disc to approximately 10–20 µm. In the final step, a GATAN 690 ion miller is used, where an ion beam further thins the sample to achieve the desired electron transparency.

The magnetic properties of the samples were analysed using the SQUID (Superconducting Quantum Interference Devices) module of an MPMS (Quantum Design, USA). The magnetization versus temperature (M-T) behaviour was investigated using Field-Cooled Warming (FCW) and Field-Cooled Cooling (FCC) protocols under an external magnetic field of 4 Tesla. Furthermore, isothermal magnetization curves (M-H) were measured by varying the magnetic field from 0 to 4 T (Tesla) across the transition temperature. Finally, DSC measurements were performed in a nitrogen atmosphere to validate the transition temperatures within the expected range for different transitions in heating as well as cooling conditions. In the present study one of the investigated alloys was used as refrigerant material to visualize the magnetocaloric effect by direct method using thermal imaging camera. The refrigerant material was exposed to low magnetic fields of 1.5 $\times 10^{-2}$ T. The thermal imaging camera (Optris PI 640i) with temperature range from – 35 °C (238 K) till 40 °C (313 K) to directly observed the magnetocaloric effect. The videos recorded are added in the subsequent section with speed 20x (20 times) to reduce the visualization time.

Table (I): XRF analysis for composition

	Ni (wt. %)	Mn (wt. %)	Ga (wt. %)
MNG-1	26.8	67.2	6.6
MNG-2	17.8	66.9	14.9
MNG-3	6.7	66.4	25.3

Methodology- Theoretical studies

The Vienna ab-initio simulation package (VASP) [24,25] is used to perform the first-principles density functional theory (DFT) calculations. The projector-augmented wave (PAW) potentials are used to describe the ion-electron [26,27] interactions in the systems. The electronic exchange and correlation part of the potential is represented by the Perdew-Burke-Ernzerhof (PBE) [28] generalized gradient approximation (GGA). The Kohn Sham orbitals are expanded using plane wave basis sets with a 500-eV energy cutoff. The conjugate-gradient algorithm is used to relax all structures until the Hellmann-Feynman forces on each atom are less than 0.005 eVÅ^{-1}. For sampling the Brillouin zone (BZ) of all MNG-1 and MNG-2 alloys, a well-converged Γ –centred Monkhorst-Pack (MP) [29] k-grids of 15×15×15. We perform AIMD analysis at different constant temperature values (using the Langevin thermostat within the canonical ensemble (NPT) [30,31] to estimate the temperatures (T_M, T_C) where structural and magnetic phase transitions occur, respectively. The AIMD simulations are run for 2 ps with a time step of 1 fs. For AIMD calculations we considered the 2×2×1 supercells both for MNG-1 and MNG-2.

Results

Microstructural features and crystal structure

The selected alloys MNG-X (X= 1, 2, 3) as shown in **Figure 1(a)** homogenized at 1073 K followed by water quenching from the broad γ phase region, exhibited the presence of the martensite as well as cubic austenite phase. A structural analysis of the chosen alloys was performed, involving XRD, SEM, and TEM studies. As shown in **Figure 1(b-g)** which shows the XRD profiles as well as SEM images obtained from the alloys quenched from the γ phase region. The analysis was performed after polishing the samples because these alloys, being rich in manganese, tended to form an oxide layer at room temperature. From these XRD profiles it was confirmed that martensite structure indicated with different symbols in **Figure 1(b, d, f)**. In the vicinity of investigated alloys, the phase transformation from cubic austenite ($L2_1$, *Fm3m*) to tetragonal martensite ($L1_0$, *P4/mmm*) phase takes place where Ga has the least concentration. The XRD peaks of MNG-1 sample are indexed to both austenite and martensite phases while for MNG-2 and MNG-3 samples peaks are indexed to only austenite phase. For MNG-1, the calculated lattice parameters for austenite phase were a = b = c = 5.32 Å and for martensite phase the lattice parameters were a = b = 5.43 Å and c = 6.30 Å which makes the c/a ratio of 1.16 as calculated from XRD profile in **Figure 1(b)**. XRD peaks of MNG-2 as shown in **Figure 1(d)** confirmed only the presence of cubic austenite phase for which the lattice parameter is a = b = c = 5.17 Å. In a similar way, XRD peaks for MNG-3 also shows the presence of only cubic austenite phase where lattice parameter is a = b = c = 5.23 Å as shown in **Figure 1(f)**.

The SEM micrographs of the ice water quenched alloys MNG-1, MNG-2 and MNG-3 are shown in **Figure 1(c)**, **(e)** and **(g)** respectively along with the EDS analysis (Shown in **Figure S1)**. As can be seen from SEM analysis, the microstructure of all the three selected alloys in single phase region which supports the thermodynamic assessment of Mn-Ni-Ga based Heusler alloy system. With the help of SEM micrograph, it is difficult to get information about the martensite which is present in investigated alloys after homogenization followed by ice water quenching. Later with the help of XRD the presence of martensite was confirmed as one can see in **Figure 1(b)** for MNG-1 which were confirmed by TEM study as shown in **Figure (2)**. Apart from the confirmation of the martensite phase and structural phase transformation also confirmed with the help of temperature-based TEM study in MNG-1 as shown in **Figure (4).**

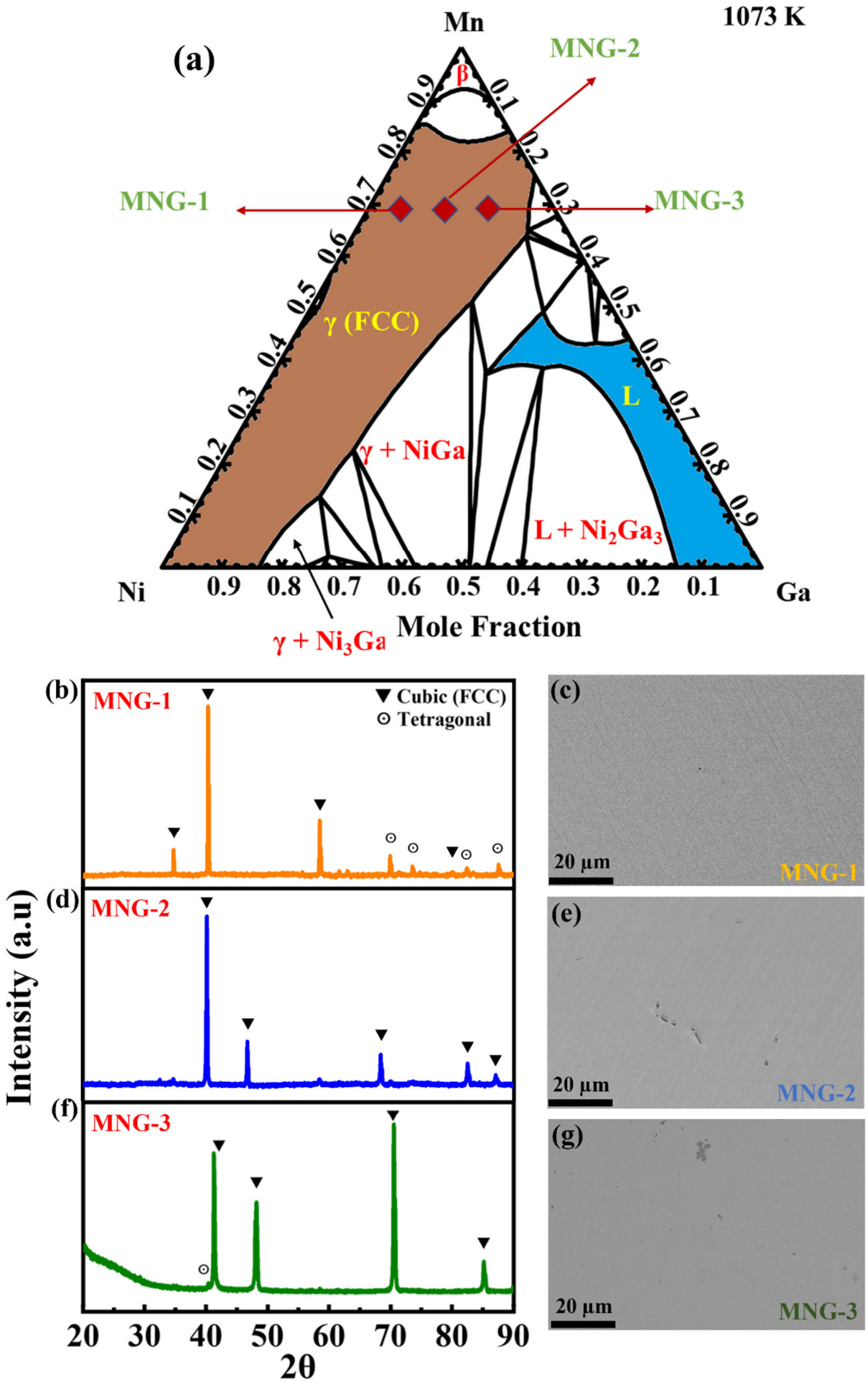

Figure 1: (a) *Isothermal section of Mn-Ni-Ga ternary alloy system at 1073 K* ***(b, c)*** *Structural features of investigated alloys –XRD profile and SEM microstructure of MNG-1.* ***(d, e)*** *XRD profile and SEM microstructure of MNG-2.* ***(f, g)*** *XRD profile and SEM microstructure of MNG-3.*

Figure 2(a) show the HR-TEM micrograph along with its selected area diffraction (SAD) along [010] axis taken in MNG-1 alloy. The diffraction spots observed in this FFT pattern can be identified as belonging to the ($L1_0$) tetragonal martensite structure, as depicted in **Figure 2(b, c),** and the FCC (L_{21}) structure shown in **Figure 2(d, e),** which confirms the cubic and ordered nature of the austenite phase. Additionally, the bright field image (BFI) in **Figure 2(f)** distinctly reveals the presence of martensite lamellae within the parent austenite phase. Additionally in **Figure S2**, the STEM image along with the compositional analysis also shown for MNG-1. For MNG-2, we also performed the TEM study along with that the corresponding FFT pattern shown in **Figure S3 (a)** which confirm the cubic austenite phase and supported the XRD study as presented in **Figure 1(d)**. Low temperature martensite phase converts into high temperature cubic austenite phase at around 250 K, this is the reason why we only confirmed the presence of cubic austenite phase. MNG-1 and MNG-2 exhibit distinct microstructural differences. TEM images show both martensite and austenite phases in MNG-1, while MNG-2 consists only of the austenite phase. MNG-1 undergoes a structural transformation near room temperature (337 K), observable by increasing beam intensity (explained in later section). In contrast, MNG-2 transforms below room temperature (252 K), explaining the absence of martensite in its images. FFT patterns further confirm these phase differences, as shown in Figure 2 and S3.

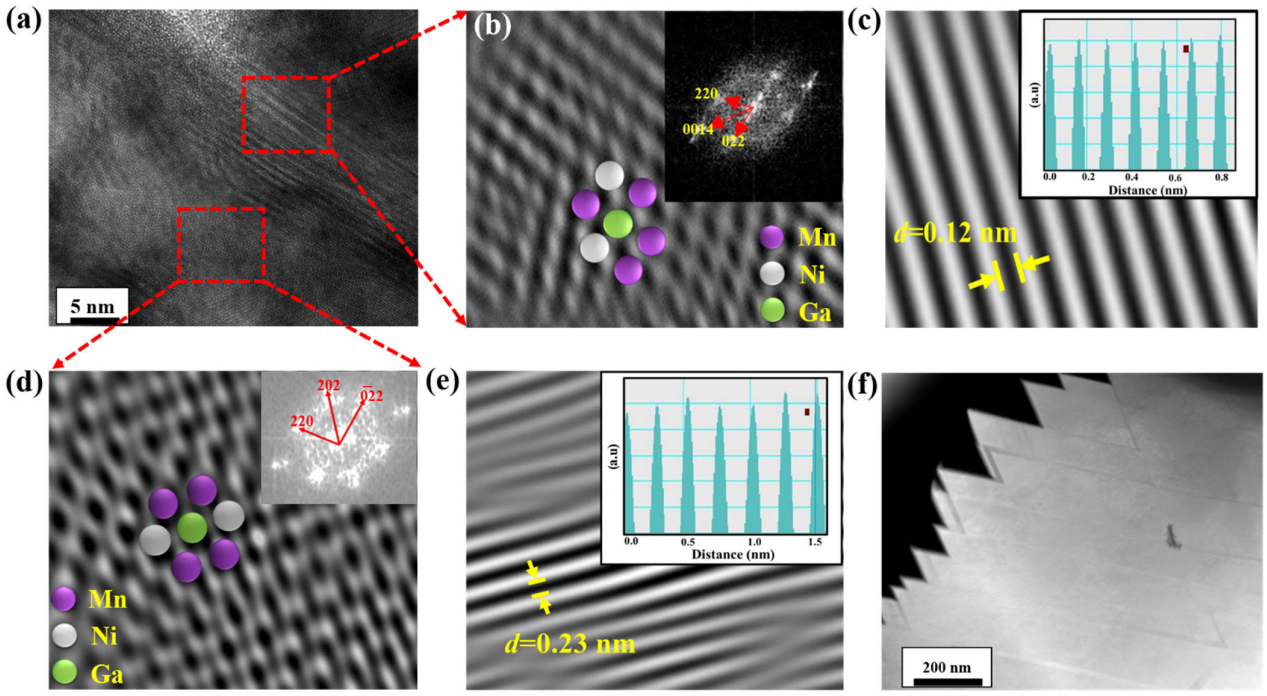

Figure 2: (a) *HR-TEM image of MNG-1* ***(b)*** *Atomic arrangements along with the FFT pattern of martensite ($L1_0$) (inset)* ***(c)*** *Corresponding lattice fringes from inverse FFT and line profile (inset)* ***(d)*** *Atomic arrangements along with the FFT pattern of austenite (L_{21}) (inset)* ***(e)*** *Corresponding lattice fringes from inverse FFT and line profile (inset)* ***(f)*** *TEM bright field image (BFI) shows lathe like structure of martensite.*

Magnetocaloric Effect

Magnetocaloric properties of all the investigated alloys were evaluated using integral of M-T behavior and M-H curves as described in **equation 1**.

$$\Delta S_T(T, H_{applied}) = \mu_0 \int_0^{H_{applied}} \left(\frac{\partial M}{\partial T}\right)_{p,H} dH \qquad (1)$$

Total entropy change (ΔS_T) is an important property to quantify among all the available magnetocaloric materials. To calculate ΔS_T, we measured the M-T plots for investigated alloys with an applied field of 4 T (Tesla). M-T plots exhibit different behaviors as the composition varies. This helps in getting information about the magnetic behavior of investigated alloy as well as transition temperatures (T_C, T_M). We then performed measurement of M-H curves in the range of transition temperatures (T_C, T_M) to calculate the magnetocaloric properties. As depicted in **Figure 3(a)**, we found the magnetic phase transition temperature (T_C) lies in the range of 315-325 K and the structural phase transition temperature (T_M) lies the range of 337-342 K in MNG-1. A sudden jump in magnetization after the T_C confirms the transformation between the martensite phase and cubic austenite phase as illustrated in **Figure S4(a)** (dM/dT versus T(K)). To confirm the phase transformation, DSC was performed and the results are presented in **Figure 3(b)**. As shown in **Figure 3(b)**, while heating MNG-1 showed the thermal arrest as an

endothermic peak at around 334 K but while cooling there is no such peak is detected. This could be due to the fact that $\Delta H^{(A\rightarrow M)}$ (austenite to martensite) is very low which causes very weak peaks in DSC. Along with that first order derivative (dH/dT) also been plotted as shown in **Figure S4(b)** confirms the structural transformation.

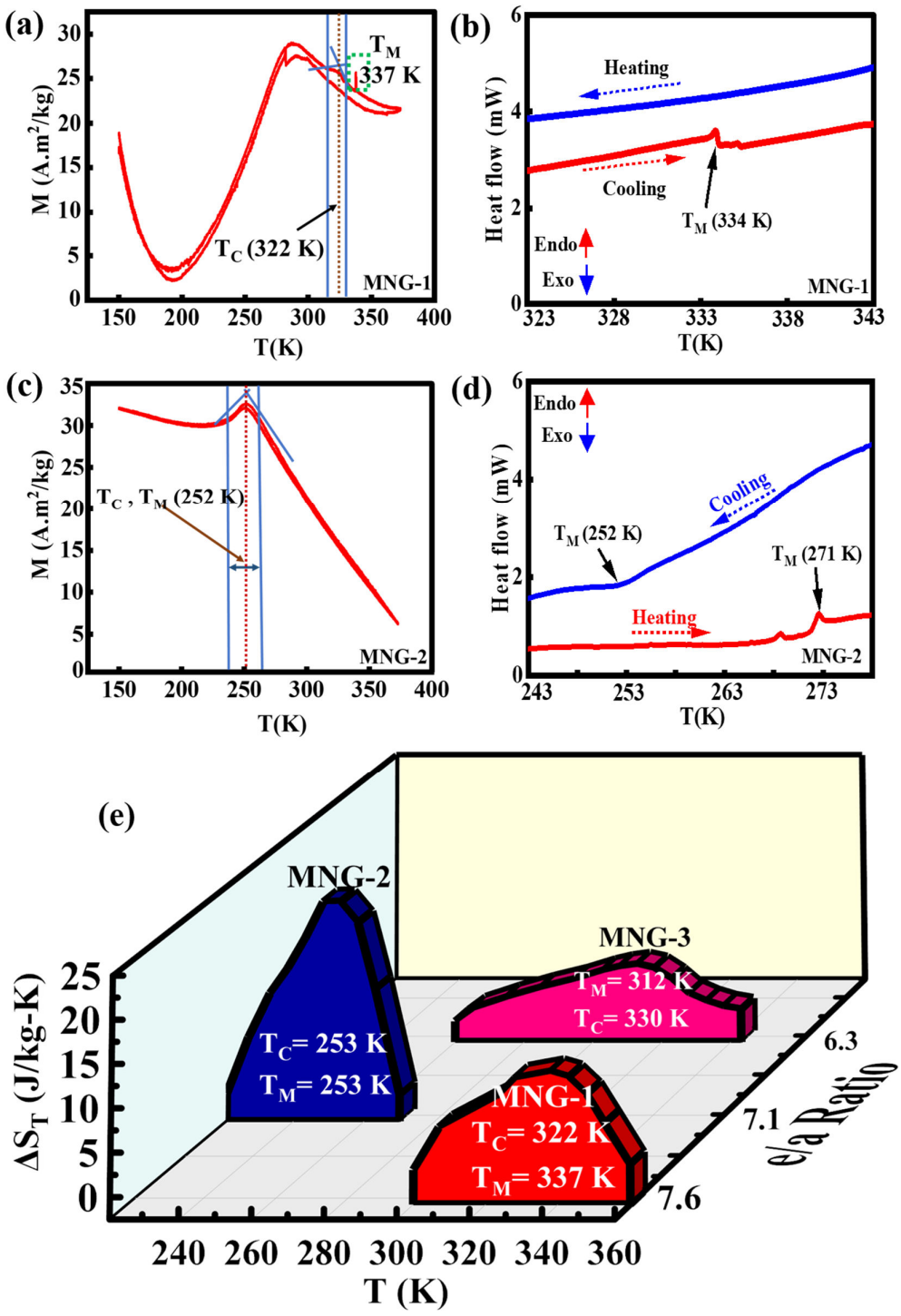

Figure 3: (a) *Magnetization versus Temperature (M-T) behavior in MNG-1 at 4 T (Tesla)* ***(b)*** *DSC curves of MNG-1 in heating and cooling mode* ***(c)*** *M-T behavior in MNG-2 at 4 T (Tesla)* ***(d)*** *DSC curves of MNG-2 in heating and cooling mode* ***(e)*** *Calculated value of ΔS_T between transition temperatures (T_C, T_M) and e/a ratio of MNG-X (X=1, 2, 3).*

For alloy MNG-2 **(Figure 3(c))**, there is a gradual increase in magnetization followed by a continuous decrease, indicating the merging of both T_C and T_M within the range of 248-256 K**.** The hysteresis between FCW and FCC cycles in the MNG-2 alloy is almost negligible compared to the other investigated alloys in this study, and a broader peak makes it the best MCM among the investigated alloys. Similarly, to confirm the phase transitions, DSC studies were performed. As shown in **Figure 3(d)**, while heating the MNG-2 alloy, a thermal arrest is observed as an endothermic peak at 271 K, and a broader exothermic peak is observed at around 253 K, confirming the M-T measurement with a thermal hysteresis of 20 K. Similarly, for MNG-2 also we have plotted dH/dT versus T (K) in **Figure S4(c)**, where one can see exothermic and endothermic peaks respectively for heating and cooling cycle. DSC analysis confirmed phase transitions, such as the martensite-to-austenite transformation, with an endothermic peak around 334 K and 270 K in MNG-1 and MNG-2 respectively. The weak DSC signal may result from unnormalized heat flow values, which, when adjusted, typically yield sharper peaks. In order to enhance peak sharpness and improve the accuracy of transition temperature identification, DSC curves and their corresponding derivative plots (dH/dT) against temperature were presented. Specifically, DSC curves and differential plots for MNG-1, MNG-2, and MNG-3 are shown in **Figure S4(b), (c)** and **Figure 5(d)** respectively with sharper peaks. Despite this, complementary techniques like HR-TEM and magnetic measurements (M-T curves) provided strong evidence of phase transitions, as explained in details in next section. While DSC alone may underrepresent these transitions, the combined data confirm both phase transformations and the magnetocaloric effect. **Figure 3(e)** shows the calculated values of ΔS_T of investigated alloys as a function of temperature (K) and valence electron per atom (e/a) ratio, which is further explained in later section.

We were also able to confirm the structural transformation with the help of HR-TEM analysis, in MNG-1. As one can see in **Figure 4(a-l),** HR-TEM images and their corresponding FFT pattern shown at different time intervals. The idea behind this to confirm the phase transformation behavior from martensite to austenite with the help of heat generated by beam intensity. To study the thermal effects on the lamellae of MNG-1, we adjusted the electron beam intensity by setting the voltage to 200 kV and the current in the range of 2-15 nA. The high-resolution transmission electron microscopy (HR-TEM) technique was employed to capture detailed images of the structural changes in MNG-1. By taking images every two seconds, one could closely monitor how the lamellae responded to the thermal variations caused by the electron beam. This approach allowed for a precise analysis of any structural transformations occurring in the material due to heating. To confirm this, we have taken many images at a fixed interval of 2 seconds but here we are only providing four images and their corresponding FFT patterns. At t_1(s) the first HR-TEM image has been taken which confirm the presence of both the martensite and austenite phase and their corresponding FFT pattern of shown in **Figure 4(b, c)** respectively. Next HR-TEM image which is taken at t_2(s) after increasing the beam intensity which causes increment in temperature shown in **Figure 4(d)**, still in this image one can see the presence of both the martensite as well as austenite phases confirmed by their corresponding FFT pattern as shown in **Figure 4(e, f).** At t_2(s), In **Figure 4(g)** the HR-TEM image and the corresponding FFT pattern in **Figure 4(h, i)** confirm the present of both martensite and austenite phases. In similar way at constant time interval, we took HR-TEM images until we arrived at austenite phase which also confirm the phase transformation as one can see in **Figure 4(j),** after occurring phase transformation we only got the austenite as shown in the corresponding FFT pattern in **Figure 4(k).** This confirms the structural phase transition from martensite to austenite phase which in later sections also confirmed by magnetic measurements as well as DSC analysis. Additionally, images obtained after cooling (t_4(s)) reveal a very small phase fraction of martensite. As seen in **Figure S5(a)** and **(c)**, the presence of martensite is confirmed. The FFT pattern in **Figure S5(d)** further verifies the martensitic phase but also shows emerging spots associated with austenite phase in the background. This is consistent with the FFT pattern (inset) in **Figure S5(b)**, which primarily indicates the presence of the austenite phase. The lower phase fraction of martensite is attributed to thermal hysteresis, a characteristic of Mn-Ni-Ga-based Heusler alloys. The presence of thermal hysteresis is already mentioned in DSC experiment, as shown in **Figure 3(b).**

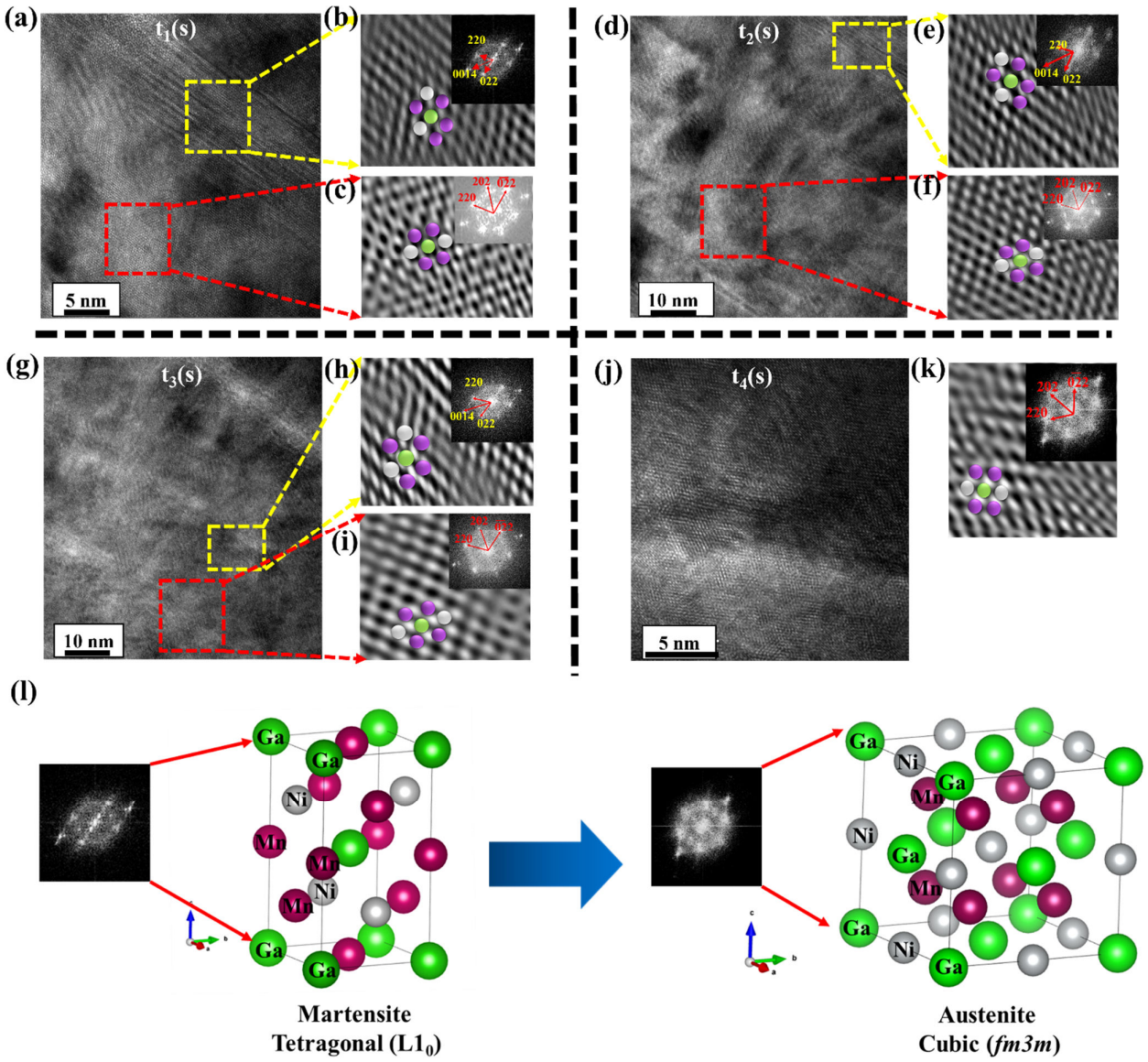

Figure 4: (a) *HR-TEM image of MNG-1 at* ***t_1(s) (b)*** *atomic arrangements of martensite (L_{10}) along with FFT pattern* ***(c)*** *Atomic arrangements of austenite (L_{21}) along with FFT pattern* ***(d)*** *HR-TEM image of MNG-1 at* ***t_2(s) (e)*** *Atomic arrangements of martensite (L_{10}) along with FFT pattern* ***(f)*** *Atomic arrangements of austenite (L_{21}) along with FFT pattern* ***(g)*** *HR-TEM image of MNG-1 at* ***t_3(s) (h)*** *Atomic arrangements of martensite (L_{10}) along with FFT pattern* ***(i)*** *Atomic arrangements of austenite (L_{21}) along with FFT pattern* ***(j)*** *HRTEM image of MNG-1 at* ***t_3(s) (k)*** *Atomic arrangements of austenite (L_{21}) along with FFT pattern* ***(l)*** *Crystal structure representation of martensite to austenite phase transformation.*

Further, alloy MNG-3, a reverse trend is observed as the magnetization increases as a function of temperature. A sudden drop in magnetization is followed by a rise and then a drop, confirming both the transition temperatures (T_M, T_C). In MNG-3, the T_M occurs approximately in the range of 308-313 K, T_C takes place within the range of 328-336 K, as shown in **Figure 5(a)**. Further we have plotted first order derivative of magnetization (dM/dT) as a function of temperature where a sudden drop in magnetization confirms the T_M as shown in **Figure 5(b)**. Transition temperature (T_C and T_M) determined using magnetic measurements (M-T and dM/dT) were also confirmed with the help of DSC, as shown in **Figure 5(c and d)**. As illustrates in **Figure 5(c),** while heating a thermal arrest as an endothermic peak is observed around 341 K, and for cooling, which was around 338 K. It is evident from the above-mentioned experimental results that Heusler alloys are highly composition-dependent, with even minor changes in concentrations of the alloying elements can lead to significant alterations in magnetic properties. The magnetocaloric effect (MCE) in Mn-Ni-Ga alloys arises from magneto-structural transitions, where the martensite-to-austenite transformation coincides with the ferromagnetic-to-paramagnetic transition. In MNG-1 and MNG-2, the alignment of Curie temperature (T_C) and structural transition temperature (T_M) leads to a significant entropy change within a narrow range. M-T curves confirm field-induced phase transitions, supported by HR-

TEM and DFT studies showing temperature-dependent lattice and magnetic moment changes. While anisotropic magnetic ordering may play a role, the primary driver of the giant entropy change is the structural transformation, validated by both experimental and theoretical data.

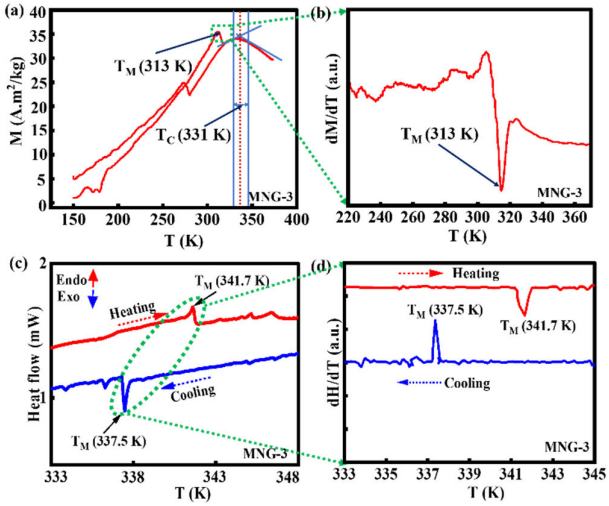

Figure 5: (a, b) *Magnetization and first order derivative (dM/dT (arbitrary units)) as a function of Temperature (M-T) in MNG-3 under the magnetic field of 4 T, respectively* ***(c, d)*** *DSC curves and first order derivative (dH/dT (arbitrary units)) of MNG-3 in heating and cooling mode, respectively.*

In **Figure S6 (a), (b), and (c)**, M-H curves are plotted for MNG-X (1, 2, 3) respectively, measured at the respective transition temperatures mentioned in the M-T curves as earlier shown in **Figure 3(a), (c), and Figure 5(a)**. The M-H curves were measured at 5-15 K intervals in the temperature ranges of 300 to 360 K for MNG-1, 225 to 265 K for MNG-2, and 260 to 350 K for MNG-3, following the described protocols [32]. To quantify ΔS_T across these transformations, we calculated it by numerically integrating Maxwell's equation as previously mentioned in **equation 1**. The calculated values, shown in **Figure 3(e)**, reveal that the maximum ΔS_T value for MNG-1 (in red) is 12.48 J/kg-K at around 340 K. Similarly, for MNG-2 (in blue), the maximum ΔS_T is around 24.50 J/kg-K, with a broad working temperature range between 240-260 K. The change in magnetic entropy (ΔS_T) correlates with the peak transition temperature, occurring where magnetic moment changes are most significant. MNG-2 exhibits strong magneto-structural coupling, with structural and magnetic transitions aligning without hysteresis, enhancing magnetocaloric properties. In contrast, MNG-1 shows weaker performance due to weak coupling, low heat flow change (ΔH), and magnetic hysteresis, which slows response to field changes. Additionally, MNG-1 has separate transition temperatures (T_C and T_M), unlike MNG-2, where they coincide. Lastly, for MNG-3 (in purple), ΔS_T is 7.61 J/kg-K, although the ΔS_T value of MNG-3 is lower compared to MNG-1 and MNG-2, it has a broader working temperature range of 290-310 K.

All three investigated alloys studied exhibit a wide operational temperature range suitable for magnetic cooling applications. This range is determined by the full width at half maximum (FWHM) in the ΔS_T with respect to temperature (K) curves for a specific magnetic field strength (H). As one can see in **Figure 3(e),** The wide working temperature range directly influences the material's performance in magnetocaloric applications. This is known as cooling capacity or refrigeration capacity (RC), which is calculated for the investigated alloys using **equation 2.**

$$RC = \Delta S_M^{Max} \times (\Delta T_{FWHM}) \quad (2)$$

The calculated RC values for the MNG-1, MNG-2 and MNG-3 are 91.38 J/Kg, 182.67 J/Kg, and 52.97 J/Kg, respectively. Although the current state of alloys shows a significant value of entropy change (ΔS_T) as well as RC, there are a few issues associated, which limits their potential. Thermal hysteresis (ΔT_h) is one amongst them as observed in Ni-Mn-X (X= Ga, Sn, In) which is associated with the magneto-structural transformation [33]. Thermal hysteresis is defined as the difference in temperature at which magneto-structural transformation occurs for heating and cooling cycle as shown in **Figure 3(b), Figure 3(d),** and **Figure 5(c)** for MNG-1, MNG-2 and MNG-3 respectively. Thermal hysteresis remains a significant limitation hindering the practical application of Heusler alloys, despite their excellent magnetocaloric properties. Various strategies have been explored to mitigate thermal hysteresis, including composition tuning and alloying with elements such as Co, Cu, and Fe[34–37]. These elements enhance the stability of martensite and austenite phases, thereby reducing thermal hysteresis. Another approach is thermal cycle pretreatment, which involves controlled thermal cycling across the structural transformation temperature range prior to application[38,39]. This process reduces hysteresis by narrowing the transformation temperature range and improving transformation reversibility[40,41]. Additionally, microstructural optimization through grain refinement is effective, achieved via methods like rapid solidification, directional solidification, or severe plastic deformation. Smaller grains reduce internal stress and accommodate transformation strains more efficiently, lowering hysteresis[42–44]. Other techniques, such as second-phase engineering, doping with rare-earth elements, and applying external stress, also help to minimize thermal hysteresis. In present study we have calculated the thermal hysteresis using the following protocols [45] and compared with the previously investigated alloys as mentioned in **Table S1**.

Furthermore, we sought to validate the proof of MCE in MNG-1 using a thermal imaging setup. It is well known that the magnetic refrigeration cycle consists of two adiabatic and two isothermal processes, while on the application of magnetic field two processes occur. Among that, first step is the temperature of magnetocaloric material increases under adiabatic condition and subsequently the material isothermally exchanges heat with the high temperature sink which is the second process. Among these processes, we focused on the initial cycle where heat is released upon the application of magnetic field, which was visualized using a thermal imaging camera. In the magnetic-refrigeration cycle illustrated in **Figure S7**, **step 1** begins with randomly oriented magnetic moments. In **step 2**, the application of an external magnetic field enhances magnetic ordering, increasing field-driven magnetic entropy and raising the temperature ($T = T_1 + T_0$). **Step 3** shows the material returning to its initial temperature as heat is removed to the ambient environment ($T = T_1$). In **step 4**, the removal of the magnetic field causes the magnetic moments to randomize, cooling the material below ambient temperature. To demonstrate the increment in temperature during the first two steps of the magnetic refrigeration cycle, we used a thermal imaging technique to showcase the magnetocaloric properties of MNG-1. The experimental setup

revealed a change in thermal gradient upon applying an external magnetic field, due to heat dissipation in **step 2**, as visualized with the thermal imaging camera. The temperature variation was demonstrated with and without DC magnetic fields.

The MNG-1 sample was positioned on the liquid nitrogen bed with an external magnetic field as shown in **Figure 6(a)** to measure thermal gradient from low temperatures (< 0 °C (~ 273 K)). Temperature was subsequently raised from -35 °C to + 40 °C (238 K to 313 K) using a hot plate, thermal images were captured at 3 °C interval. The observation focused on the transition temperatures (T_C, T_M), and aimed to observe temperature changes in the material within the critical transition range. Initially, **Figure 6(b)** shows observations made at this temperature range without the application of magnetic field. In the second series of experiments, **Figure 6(c)**, small magnetic fields were applied using a neodymium magnet block (1.5 $\times 10^{-3}$ T), on which the sample was positioned, and the entire setup placed on a liquid nitrogen bed.

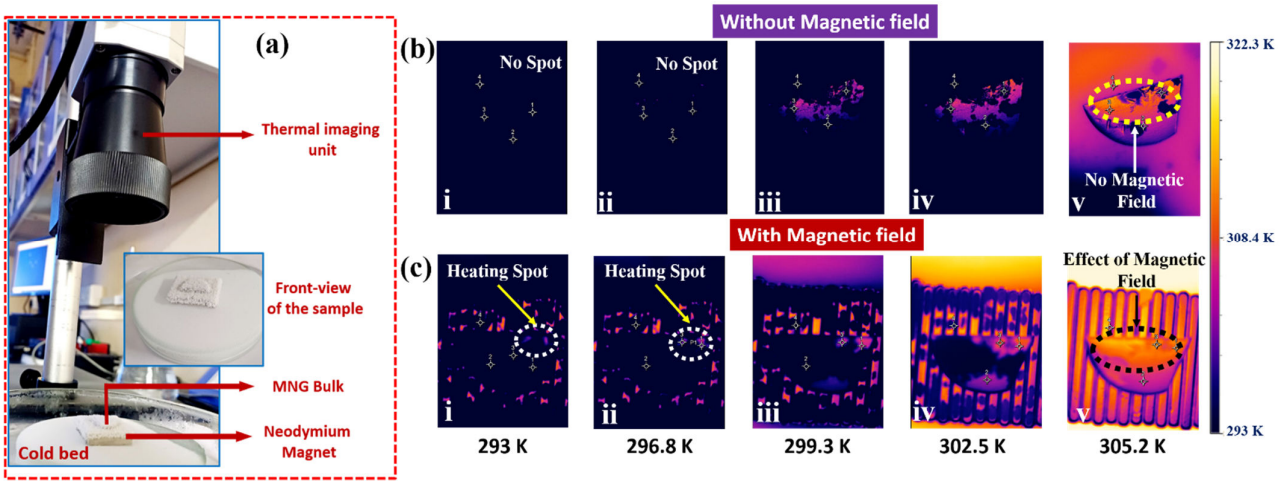

Figure 6: (a) *Experimental set up of thermal imaging camera for MNG-1* ***(b)*** *Thermal images of MNG-1 without any external magnetic field at different temperatures* ***(c)*** *Thermal images of MNG-1 under the influence of external magnetic field at different temperatures.*

To elaborate, **Figure 6(b) (i – v)** shows gradual heating in MNG-1 without magnetic field within the temperature range of 20 °C to 35 °C (293 K to 305 K) and no specific trap states were observed. Additionally, the thermal gradient between the surrounding liquid nitrogen bed and the material remained at a consistent temperature difference of ~ 2 °C. **Video S1** clearly demonstrates the behaviour of material while heating at transition temperatures ranging from 20 °C to 35 °C (lower temperatures cannot be imaged due to colour scheme pertaining to thermal imaging camera). Later, thermal gradient observations from images taken at the same temperature range in the presence of magnetic field are shown in **Figure 6(c)**. When comparing MNG-1 at 20 °C (~293 K), **Figure 6(b) (i) and (c) (i)** reveal thermal gradient (Heating spots), but as the temperature increases, the difference in thermal gradient becomes noticeable. At 23.8 °C (~296.8 K) and 28.6 °C **(Figure 6(c) (ii – iv))**, a substantial thermal gradient was observed in the presence of an external magnetic field. The SQUID experimental data showed temperature-dependent magnetization transitions in the range of 315 - 325 K, as depicted in **Figure 3(a)** and **(e)**. A noticeable temperature difference exists between the SQUID experimental data and the thermal imaging analysis, which can be attributed to the simultaneous application of heat and varied magnetic field externally. Since this is a prototype experimental setup placed at non-controllable atmosphere, these factors may contribute to the temperature variance observed between the SQUID and thermal imaging analyses of MNG-1. In addition to the thermal gradient, with a temperature difference of > 3 °C from the surroundings (on magnet), the images exhibit thermal spots at lower temperatures. We presume that these spots represent trap states that exhibit higher temperatures at a faster rate on exposure to higher magnetic field. This serves as a direct proof of concept of a magnetocaloric heating cycle near room temperature.

Discussion

Mn-Ni-Ga alloys, known for their giant magnetocaloric effect (GMCE), exhibit sensitivity to their composition. This effect is attributed to a magneto-structural transformation, where both magnetic and structural transitions occur over a broad temperature range, significantly enhancing the magnetocaloric response (as shown in **Figure 3(c)**). As previously noted, Heusler alloys are highly sensitive to compositional changes. Even slight adjustments can significantly affect the transformation temperatures (T_C and T_M) and magnetocaloric properties. The transition temperatures (T_C, T_M) can be significantly shifted by tuning the alloy composition, as depicted in **Figure 3(a-e) and Figure 6(a-d)**. To establish a link between these factors, numerous studies have investigated the connection between magnetocaloric behaviour and the electron-to-atom (e/a) ratio. The e/a ratio represents the average number of valence electrons contributed by each atom in an alloy, serving as a key parameter to understand the material's electronic, structural, and magnetic properties[46,47]. This calculation illustrates a direct relationship between the composition of the alloys and their functional properties[48]. While the e/a ratio itself is not a new concept, its use as a tool to predict and correlate magnetocaloric properties in Heusler alloys is a simple yet effective approach. A clear relationship

between the e/a ratio and magnetocaloric properties provides a useful framework for designing materials and compositions with optimal magnetocaloric performance[49,50]. In **Figure 3(e)**, the different transition temperatures (T_C, T_M) for MNG-1, MNG-2, and MNG-3 are shown alongside their corresponding electronic configurations (e/a ratio). Among these transitions, the structural phase transition has a direct relationship with the e/a ratio and significantly contributes to the ΔS_T value. This transition entails the material shifting from martensite phase to cubic austenite phase with increased symmetry. It is a diffusion less transformation, wherein atoms reorganize via a shear-like mechanism while retaining their positions [51]. In Mn-Ni-Ga ternary Heusler alloys, the structural phase transition is induced by Jahn-Teller distortion, which causes electronic instabilities in the austenite phase [52]. These changes in crystal structure initiate a redistribution of electrons among d-sub bands of both symmetries, helping to mitigate these instabilities. The extent of p-d orbital hybridization between the p states of Ga atoms and the d states of Mn atoms also influences the structural transformation temperature (T_M) [21,53,54]. As mentioned, the electron configuration which is available for p-d orbital hybridization changes, which is expressed in the form of e/a ratio.

This study examines impact of stoichiometric changes on magnetocaloric properties by correlating structural phase transitions with the e/a ratio. As shown in **Figure 3(e)**, the magnetic phase transition temperature (T_C) and structural transformation temperature (T_M) align within a specific composition range for Gallium (Ga) content ranging from 5 at. % to 25 at. % (equivalent to an e/a value between 6.3 and 7.59). The compositions analysed in this study, shown in **Figure 3(e)**, demonstrate an increase in gallium (Ga) at the cost of nickel (Ni), as nickel has 10 electrons in its outer shell compared to gallium's 3. This shift results in an overall decrease in electron contribution, leading to a reduction in the e/a ratio. For MNG-1, the e/a ratio is at its maximum, around 7.6, resulting in the T_M and T_C occurring within a narrow range with minimal hysteresis. Similarly, MNG-2 alloy shows the highest ΔS_T value which is attributed to the magneto-structural transition and the absence of hysteresis, which contributes to the GMCE in Heusler alloys. The e/a ratio for MNG-2 was around 7.1, resulting in T_M and T_C occurring within a single temperature range, making it favourable for GMCE applications. MNG-3 exhibits the least magnetocaloric properties, with an e/a ratio of less than around 6.3 and a wide temperature difference between both T_C and T_M. Additionally, a wide hysteresis, as mentioned earlier, leads to poor values of ΔS_T and refrigeration capacity (RC). Further we have summarized the e/a ratio along with the T_C and T_M values of the investigated alloys in Table (II). The anticipated range of e/a ratio in manganese-rich Mn-Ni-Ga based alloys for magneto-structural transformations is between 6.9 and 7.2, as demonstrated in this study. In contrast, for nickel-rich alloys, this transformation occurs between 7.4 and 7.7 [55].

Table (II): The e/a ratio and transition temperature (T_C, T_M) value of investigated alloys.

Alloys	e/a Ratio	T_C (K)	T_M (K)
MNG-1	7.6	322	337
MNG-2	7.1	252	252
MNG-3	6.3	331	313

In this study, we compare the ΔS_T values with those of previously investigated Mn-Ni-Ga based alloys, as illustrated in **Figure 7(a)**. The figure presents the ΔS_T values plotted against temperature (K) and magnetic field (Tesla) from prior studies [56–68] in comparison to current work. It is quite evident that despite the ΔS_T values being calculated at 4 T (Tesla) in this study, the investigated alloys exhibit better magnetocaloric properties than the standard magnetocaloric materials, where the ΔS_T is calculated at various magnetic field (Tesla).

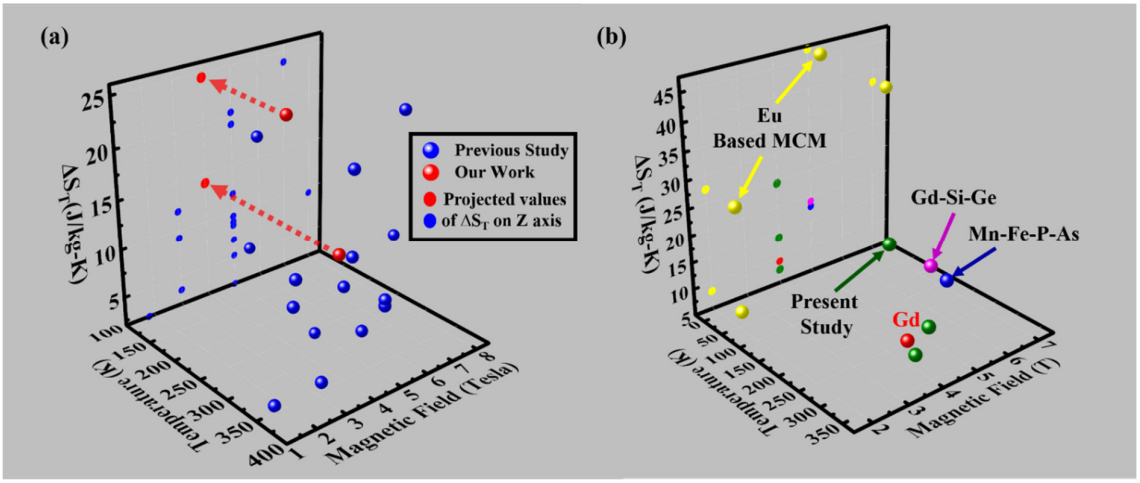

***Figure 7**: **(a)** Magnetocaloric properties of previous studies in comparison to current work [56–68] and **(b)** Comparison of investigated alloys (green) with other standard magnetocaloric materials (MCM) [5,9,14,69–73].*

Along with this, as mentioned in **Figure 7(b)** magnetocaloric properties of Gd, Gd-Si-Ge, Mn-Fe-P-As and Eu based alloys and oxide also compared with present work. As one can see in **Figure 7(a),** Gd has the value of ΔS_T around 9.3 J/kg-K at 298 K and Gd-Si-Ge has 19 J/kg-K at 270 K under the magnetic field of 5 T [5,9]. While Mn-Fe-P-As alloys shows around 18 J/kg-K at 305 K under the magnetic

field of 5 T [14]. Although, Eu based oxides shows promising magnetocaloric properties (ΔS_T~ 28 J/kg-K) at small magnetic fields (2 T) suitable MCM for magnetic refrigeration [69–72]. This suggests that the values of ΔS_T and RC of the investigated alloys are comparable with other reported rare earth-based alloys and some of the other stoichiometric Heusler alloys [73]. Additionally, DFT calculations were performed to support the structural and magnetic behaviour of the investigated alloy. For MNG-3, this study includes only experimental details to illustrate the impact of composition on magnetocaloric properties. Due to its relatively poor performance, DFT calculations were not carried out for MNG-3. However, DFT calculations were conducted exclusively for MNG-1 and MNG-2, as they demonstrated the promising magnetocaloric properties.

Theoretical calculations for magnetic and structural properties

The possible theoretical crystal structure of the experimentally selected MNG-1 alloy is shown in **Fig 8(a)**. There is 11 Mn, 4 Ni, and 1 Ga atoms in the unit cell, which is close to the experimental composition of MNG-1. The equilibrium lattice parameter for the relaxed MNG-1 is *a* = 5.96 Å.

To get insight into the structural as well as the magnetic phase transitions of MNG-1 we further perform AIMD calculations on DFT relaxed structures. The structural evolution of MNG-1 after 2 ps of AIMD simulation at temperatures T_1 = 150, 200, 250, 300, 322, and 350K are shown in **Fig 8 (a(i-vi)**, respectively. A substantial atomic displacement of atomic positions is observed, leading to a significant modification of lattice parameters. **Figure 8 (a(viii))** (red dotted line with solid red circles) shows the change in lattice parameter (*a*) of MNG-1 under different temperatures. The lattice parameter starts increasing with an increase in temperature up to 350 K. However, there is a sudden drop in the lattice parameter after 350 K. This suggests a structural phase transition in MNG-1 at T_M = 350K. Moreover, the value of ΔS_T in a system is related to the structural transformation, and therefore, ΔS_T also occurs near T_M. The DFT simulated value of T_M is very close to the experimental result where structural phase transformation for MNG-1 occurs at 337 K (**Figure 3(a))**.

To calculate the T_C, we further analyze the magnetic ground states of MNG-1 using spin-polarized DFT [74–76]. We find that MNG-1 shows the Ferromagnetic (FM) ground state. **Figure 8(a(vii))** shows the spin-projected density of states (DOS) for MNG-1 under FM ground state. The d orbitals of Mn and Ni contribute most significantly to the total DOS. The minority (spin-down) and the majority (spin-up) DOS are represented in the lower and upper parts, respectively, in **Figure 8 (a(vii)).** For Ni atoms, most of the energy levels for electrons with both spin orientations (up and down) lie below the Fermi level. The Ni atoms exhibit near-equal spin-up and spin-down occupancy, shows a negligible net magnetic moment. While for Mn atoms, spin-up states occupy the energy levels below the Fermi level. Conversely, the energy bands for spin-down electrons exhibit a peak positioned above the Fermi level. Therefore, the Mn atoms (magnetic moment of 3.392 μ_B per Mn atom) mostly contribute to total magnetic moment of the alloy system. However, the change in structure of MNG-1 with temperatures could result in modulation in the magnitudes of these magnetic moments. We, therefore, calculated the magnetic moment values for each crystal structure at different temperatures (T_1) mentioned above. The magnetic moment variation with different temperatures is shown in **Figure 8 (a(viii)).** The magnitude of the magnetic moment increases with temperatures; however, after 322 K, there is a sudden decrease in magnetic moment. This further indicates that the magnetic phase transformation for MNG-1 occurs at 322 K, which is consistent with the experimentally observed Curie temperature.

Figure 8(b) represents the DFT relaxed structure of the MNG-2 alloy with 11 Mn atoms, 3 Ni atoms, and 2 Ga atoms which is close to the experimental composition of MNG-2. The equilibrium lattice parameter of the optimized structure is *a* = 5.21 Å. **Figure 8 (b(i-vi)** represents the DFT relaxed structures of MNG-2 for temperatures T= 100, 150, 200, 230, 240 and 250 K, respectively. From the optimized structures of MNG-2, it can be observed that there is a change in atomic orientations and the displacements between two atoms with different temperature values. This results in a change in lattice parameter values, the variation in lattice parameter (*a*) with temperature for MNG-2 is shown in **Figure 8 (b(viii)).** There is a sharp drop in the lattice parameter, hence in ΔS_T just after temperature T_M = 230 K. This obtained temperature value is very close to the experimentally observed T_M = 252 K **(Figure 3(c))**. Like MNG-1, we find that MNG-2 also exhibits the FM ground state. The spin-projected DOS of MNG-2 is shown in **Figure 8 (b(vii)).** The electron states from *d* orbitals of Mn and Ni atoms largely contribute near the Fermi level. The spin-up (down) states of Mn atoms are mostly situated below (above) the Fermi level. In contrast to Ni atoms where the maximum spin-up and -down states lie below the Fermi level, the Mn atoms (2.54 μ_B per Mn atom) mostly contribute in the total magnetic moment of MNG-2. To determine the Curie temperature T_C value for MNG-2, we further calculate the magnetic moments of the crystal structures corresponding to different temperatures. The magnetic moment per unit cell of MNG-2 increases up to 240 K and suddenly drops after 240 K, indicating that the curie temperature T_C = 240 K as shown in **Figure 8 (b(viii))** which is nearby to the experimentally determined T_C.

Theoretical studies were performed for the two best performing magnetocaloric alloys, MNG-1, and MNG-2. In MNG-1, experimentally both the transition temperatures (T_C, T_M) were around 337 K and 322 K respectively. Similarly, also for MNG-2, both the transition temperatures were in the same range which was around 253 K, which by theoretical calculations were within the range of 240-250 K. Although there is temperature difference of 10-20 K which is due to that the externally applied magnetic field is not considered while analyzing DFT studies.

As in the current work we have explored the magnetocaloric properties extensively by using experimental and theoretical methods. But from the application point of view of MCM, mechanical behaviour is also equally important. Brittleness of Mn-rich alloys is acknowledged, and to enhance their mechanical properties, a recent study introducing Cu in Mn-Ni based alloys is performed. This substitution improved the mechanical properties, making the alloys more ductile compared to Mn-Ni-Ga based alloys[76]. Apart from this, currently all *d* metal type Heusler alloys are also using to improve the mechanical properties[77]. This balance between magnetic and mechanical properties is crucial for tailoring these materials for specific applications, where optimizing both factors is essential for practical use. The present work emphasizes optimizing compositions to reduce thermal hysteresis and improve refrigeration capacity, while mechanical property investigation is not the focus. Despite challenges, Mn-rich Mn-Ni-Ga alloys demonstrate impressive magnetocaloric performance near room temperature, with significant ΔS_T values.

ARTICLE

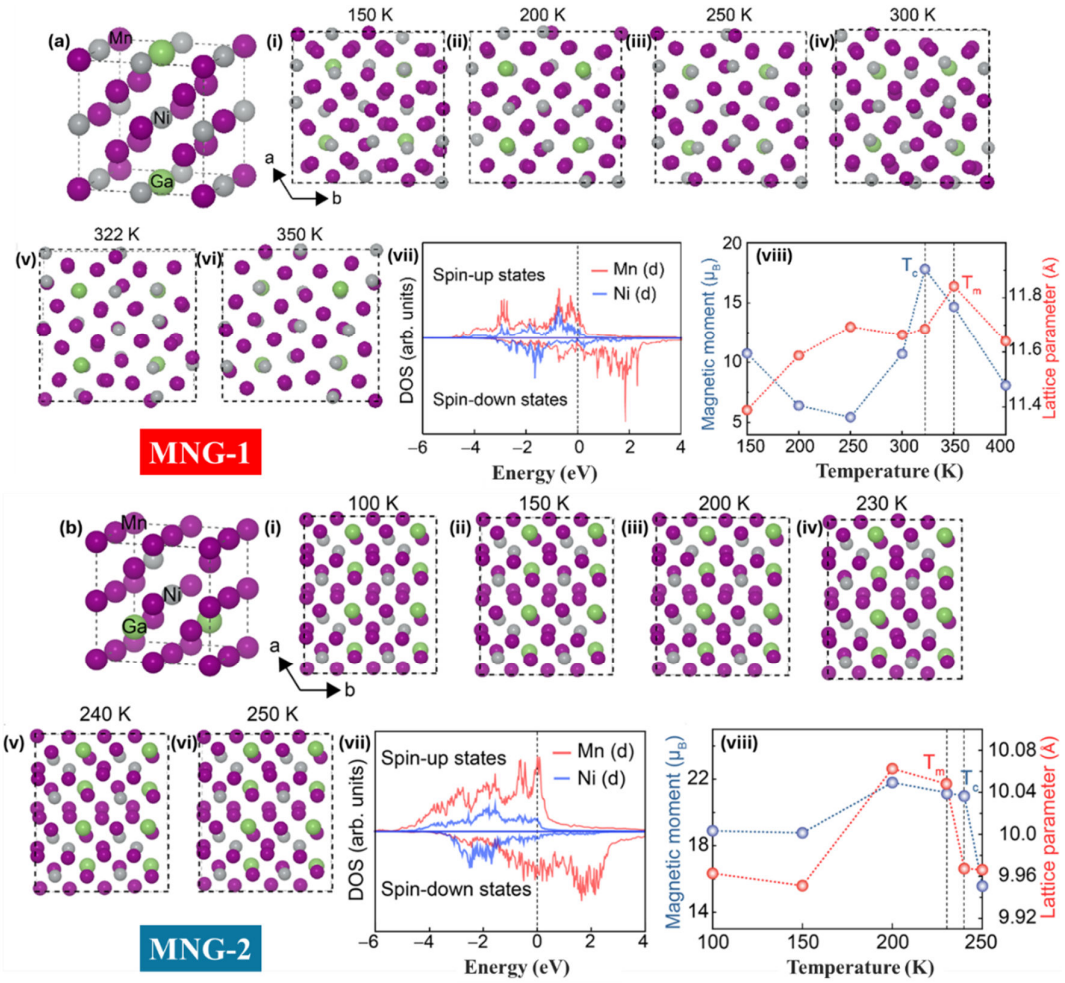

Figure 8: (a) *The DFT simulated optimized crystal structure of MNG-1.* ***a(i-vi))*** *The top views of MNG-1 after 2 ps of AIMD simulation at temperatures 150, 200, 250, 300, 322, and 350 K, respectively.* ***a(vii)*** *The spin-projected DOS for MNG-1. The upper and lower panel of DOS represent the spin-up and –down states, respectively.* ***a(viii)*** *The variation of magnetic moment and equilibrium lattice parameter of optimized MNG-1 at different temperatures.* ***(b)*** *The DFT simulated optimized crystal structure of MNG-2.* ***b(i-vi))*** *The top views of MNG-2 after 5 ps of AIMD simulation at temperatures 100, 150, 200, 230, 240 and 250 K, respectively.* ***b(vii)*** *The spin-projected DOS for MNG-2. The upper and lower panel of DOS represent the spin-up and –down states, respectively.* ***b(viii)*** *The variation of magnetic moment and equilibrium lattice parameter of optimized MNG-2 at different temperatures.*

Conclusion

In this study, Mn-rich Heusler alloys show exceptional magnetocaloric properties for room temperature applications. The alloy composition was formulated to keep the manganese (Mn) content constant while adjusting the nickel (Ni) and gallium (Ga) content, utilizing the CALPHAD thermodynamic database for the Mn-Ni-Ga ternary system. A combined analysis of experimental and theoretical data revealed the stoichiometric influence on the Heusler alloy. Experimental analysis of MNG-1 alloy revealed the existence of martensite, a finding that was validated through HR-TEM. In-situ HR-TEM studies also confirmed the structural phase transition from the martensite phase to the austenite phase in MNG-1. Likewise, XRD profiles and SEM analysis of MNG-2 and MNG-3 confirmed a single phase, a finding that was also confirmed by HR-TEM. Magnetic measurements including magnetization versus temperature (M-T) and M-H behaviour were conducted using to study the magnetocaloric properties. DSC experiments are conducted in both

cooling as well as heating condition which also supported the M-T study. Among the alloys, MNG-1 exhibited a significant entropy change (ΔS_T) of around 12.48 J/kg-K and a refrigeration capacity (RC) of approximately 91.38 J/kg. MNG-2 displayed remarkable properties attributed to a magneto-structural transformation, with ΔS_T around 24.50 J/kg-K and an RC of about 182.67 J/kg. Both MNG-1 and MNG-2 exhibited superior magnetocaloric properties compared to other conventional rare-earth-element-based alloys. In contrast, MNG-3 showed the least magnetocaloric properties due to a large temperature hysteresis, with ΔS_T around 7.61 J/kg-K and an RC of approximately 52.97 J/kg. We have also directly visualized the MCE for one of the alloys (MNG-1) using thermal imaging setup. Density functional theory (DFT) calculations were also performed for MNG-1 and MNG-2 to estimate the transition temperatures (T_C, T_M), which agreed well with the experimental values. The application of this integrative approach of experimental and theoretical studies of Heusler alloys will help in exploring composition for specific application.

Author contributions

Conceptualization, Data curation, Formal analysis, Methodology, Writing-original draft: NT and SM; Software, Validation, Resources: AKS, SS and MP; Funding, Supervision, Writing-review, and editing: ST, MP, and CST.

Conflicts of interest

"There are no conflicts to declare."

Data availability

The raw/processed data required to reproduce these findings cannot be shared at this time as the data also forms part of an ongoing study.

Acknowledgements

C.S.T acknowledges Core research grant of SERB, India, STARS projects by MHRD-India, DAE Young Scientist Research Award (DAEYSRA), and the AOARD (Asian Office of Aerospace Research and Development) grant no. FA2386-21-1-4014, and Naval research board for funding support. S. T acknowledges support from the U.S. Department of Energy (Grant No., DE-FG02-06ER46291).

References

1 O. Gutfleisch, M. A. Willard, E. Brück, C. H. Chen, S. G. Sankar and J. P. Liu, *Advanced Materials*, 2011, **23**, 821–842.

2 W. Gao, R. Brennan, Y. Hu, M. Wuttig, G. Yuan, E. Quandt and S. Ren, *Materials Today*, 2018, **21**, 771–784.

3 T. Gottschall, K. P. Skokov, M. Fries, A. Taubel, I. Radulov, F. Scheibel, D. Benke, S. Riegg and O. Gutfleisch, *Adv Energy Mater*, DOI:10.1002/aenm.201901322.

4 B. G. Shen, J. R. Sun, F. X. Hu, H. W. Zhang and Z. H. Cheng, *Advanced Materials*, 2009, **21**, 4545–4564.

5 K. A. Gschneidner and V. K. Pecharsky, *Annu. Rev. Mater. Sci.*, 2000, 387–429.

6 Q. Liu, J. Wang, H. Xie, Q. Fu, X. Q. Gao, Z. Li, J. L. Zhao and Z. Mo, *J Alloys Compd*, DOI:10.1016/j.jallcom.2022.168372.

7 H. Xie, Q. Liu, X. Luo, S. Ma, X. Gao, Z. Li, Z. Mo and J. Shen, *J Alloys Compd*, DOI:10.1016/j.jallcom.2022.167623.

8 V. Smetana, Y. Mudryk, V. K. Pecharsky and A. V. Mudring, *J Mater Chem C Mater*, 2018, **6**, 1353–1362.

9 V. K. Pecharsky and K. A. Gschneidner, *Phys Rev Lett*, 1997, **78**, 4494–4497.

10 Y. Sutou, Y. Imano, N. Koeda, T. Omori, R. Kainuma, K. Ishida and K. Oikawa, *Appl Phys Lett*, 2004, **85**, 4358–4360.

11 T. Krenke, E. Duman, M. Acet, E. F. Wassermann, X. Moya, L. Manosa and A. Planes, *Nat Mater*, 2005, **4**, 450–454.

12 S. Sun, H. Qin, H. Wang, R. Ning, Y. Zhao, J. Zhu, Z. Gao, D. Cong, Y. Wang and W. Cai, *Mater Today Energy*, DOI:10.1016/j.mtener.2020.100533.

13 F. X. Hu, B. G. Shen, J. R. Sun, Z. H. Cheng, G. H. Rao and X. X. Zhang, *Appl Phys Lett*, 2001, **78**, 3675–3677.

14 O. Tegus, E. Brueck, K. H. J. Buschow and F. R. de Boer, *ChemInform*, 2002, **33**, 150–152.

15 T. Graf, C. Felser and S. S. P. Parkin, *Progress in Solid State Chemistry*, 2011, **39**, 1–50.

16 K. Mandal, D. Pal, N. Scheerbaum, J. Lyubina and O. Gutfleisch, 2008, **44**, 2993–2996.

17 L. Righi, F. Albertini, E. Villa, A. Paoluzi, G. Calestani, V. Chernenko, S. Besseghini, C. Ritter and F. Passaretti, *Acta Mater*, 2008, **56**, 4529–4535.

18 J. Pons, R. Santamarta, V. A. Chernenko and E. Cesari, *J Appl Phys*, DOI:10.1063/1.1861137.

19 V. Chemenko, *Scr Mater*, 1999, **40**, 523–527.

20 G. Li, L. Xu and Z. Cao, *J Mater Chem C Mater*, 2023, **11**, 6173–6182.

21 S. Roy, E. Blackburn, S. M. Valvidares, M. R. Fitzsimmons, S. C. Vogel, M. Khan, I. Dubenko, S. Stadler, N. Ali, S. K. Sinha and J. B. Kortright, *Phys Rev B Condens Matter Mater Phys*, 2009, **79**, 1–5.

22 J. Duan, P. Huang, H. Zhang, Y. Long, G. Wu, Rongchang Ye, Y. Chang and Farong Wan, *J Magn Magn Mater*, 2007, **309**, 96–99.

23 N. Tiwari, V. Pal, S. Das and M. Paliwal, *J Electron Mater*, DOI:10.1007/s11664-023-10882-0.

24 G. Kresse and J Furthmuller, *Phys. Rev. B*, 1996, **54**, 11169.

25 G. Kresse and J. Furthmüller, *Comput Mater Sci*, 1996, **6**, 15–50.

26 J. P. Perdew, K. Burke and M. Ernzerhof, *Phys Rev Lett*, 1997, **78**, 1396–1396.

27 P. E. Blöchl, *Phys Rev B*, 1994, **50**, 17953–17979.

28 G. Kresse and D. Joubert, *Phys Rev B*, 1999, **59**, 1758–1775.

29 Hendrik J. Monkhorst and James D. Pack, *Phys Rev B*, DOI:10.1039/c8ta11250a.

30 W. G. Hoover, A. J. C. Ladd and B. Moran, *Phys Rev Lett*, 1982, **48**, 1818–1820.

31 B. L. Holian and D. J. Evans, *J Chem Phys*, 1983, 5147–5150.

32 V. Franco and B. Dodrill, *Magnetic Measurement Techniques for Materials Characterization*, 2021.

33 V. Franco, J. S. Blázquez, J. J. Ipus, J. Y. Law and A. Conde, *Prog Mater Sci*, 2018, **93**, 112–232.

34 Y. Zhang, J. Bai, K. Guo, D. Liu, J. Gu, N. Morley, Q. Ma, Q. Gao, Y. Zhang, C. Esling, X. Zhao and L. Zuo, *J Alloys Compd*, DOI:10.1016/j.jallcom.2024.173593.

35 Y. Sokolovskaya, O. Miroshkina, D. Baigutlin, V. Sokolovskiy, M. Zagrebin, V. Buchelnikov and A. T. Zayak, *Metals (Basel)*, DOI:10.3390/met11060973.

36 C. Seguí, J. Torrens-Serra, E. Cesari and P. Lázpita, *Materials*, DOI:10.3390/ma13020419.

37 A. A. Mendonça, L. Ghivelder, P. L. Bernardo, H. Gu, R. D. James, L. F. Cohen and A. M. Gomes, *Phys Rev Mater*, DOI:10.1103/PhysRevMaterials.4.114403.

38 A. Wederni, M. Ipatov, M. Khitouni and J. J. Suñol, *J Therm Anal Calorim*, DOI:10.1007/s10973-023-12580-9.

39 Y. Q. Ma, C. B. Jiang, G. Feng and H. B. Xu, *Thermal stability of the Ni 54 Mn 25 Ga 21 Heusler alloy with high temperature transformation*, .

40 O. Gutfleisch, T. Gottschall, M. Fries, D. Benke, I. Radulov, K. P. Skokov, H. Wende, M. Gruner, M. Acet, P. Entel and M. Farle, *Philosophical Transactions of the Royal Society A: Mathematical, Physical and Engineering Sciences*, DOI:10.1098/rsta.2015.0308.

41 A. L. Pires, J. H. Belo, I. T. Gomes, A. M. L. Lopes, J. P. Araújo, A. M. Pereira, R. L. Hadimani, D. C.

Jiles, D. L. Schlagel and T. A. Lograsso, *Thin Solid Films*, 2017, **621**, 247–252.

42 J. Guo, M. Zhong, W. Zhou, Y. Zhang, Z. Wu, Y. Li, J. Zhang, Y. Liu and H. Yang, *Materials*, DOI:10.3390/ma14092339.

43 L. Pfeuffer, J. Lemke, N. Shayanfar, S. Riegg, D. Koch, A. Taubel, F. Scheibel, N. A. Kani, E. Adabifiroozjaei, L. Molina-Luna, K. P. Skokov and O. Gutfleisch, *Acta Mater*, DOI:10.1016/j.actamat.2021.117390.

44 S. Ma, X. Zhang, G. Zheng, M. Qian and L. Geng, *Multidisciplinary Digital Publishing Institute (MDPI)*, 2023, preprint, DOI: 10.3390/ma16165725.

45 C. Zhang, X. Chen, O. Hubert and Y. He, *Materialia (Oxf)*, DOI:10.1016/j.mtla.2024.102038.

46 A. Planes, L. Mãosa and M. Acet, *Journal of Physics Condensed Matter*, DOI:10.1088/0953-8984/21/23/233201.

47 A. Taubel, B. Beckmann, L. Pfeuffer, N. Fortunato, F. Scheibel, S. Ener, T. Gottschall, K. P. Skokov, H. Zhang and O. Gutfleisch, *Acta Mater*, 2020, **201**, 425–434.

48 X. Jin, M. Marioni, D. Bono, S. M. Allen, R. C. O'Handley and T. Y. Hsu, *J Appl Phys*, 2002, **91**, 8222–8224.

49 B. Gao, J. Shen, F. X. Hu, J. Wang, J. R. Sun and B. G. Shen, *Appl Phys A Mater Sci Process*, 2009, **97**, 443–447.

50 X. Zhou, H. Kunkel, G. Williams, S. Zhang and X. Desheng, *J Magn Magn Mater*, 2006, **305**, 372–376.

51 Khachaturyan Armen. G, *Theory of Structural Transformations in Solids*, 2013.

52 P. J. Brown, A. Y. Bargawi, J. Crangle, K. U. Neumann and K. R. A. Ziebeck, *Journal of Physics Condensed Matter*, 1999, **11**, 4715–4722.

53 G. J. Li, E. K. Liu, H. G. Zhang, Y. J. Zhang, G. Z. Xu, H. Z. Luo, H. W. Zhang, W. H. Wang and G. H. Wu, *Appl Phys Lett*, DOI:10.1063/1.4791701.

54 T. Krenke, X. Moya, S. Aksoy, M. Acet, P. Entel, L. Mañosa, A. Planes, Y. Elerman, A. Yücel and E. F. Wassermann, *J Magn Magn Mater*, 2007, **310**, 2788–2789.

55 V. Franco, J. S. Blázquez, J. J. Ipus, J. Y. Law and A. Conde, *Prog Mater Sci*, 2018, **93**, 112–232.

56 R. A. Booth and S. A. Majetich, *J Appl Phys*, 2012, **111**, 1–4.

57 U. Devarajan, S. Esakki Muthu, S. Arumugam, S. Singh and S. R. Barman, *J Appl Phys*, 2013, **114**, 0–6.

58 S. Singh, S. Esakki Muthu, A. Senyshyn, P. Rajput, E. Suard, S. Arumugam and S. R. Barman, *Appl Phys Lett*, DOI:10.1063/1.4863742.

59 L. Wei, X. Zhang, W. Gan, C. Ding, C. Liu, L. Geng and Y. Yan, *J Alloys Compd*, 2021, **874**, 159755.

60 S. Datta, S. S. Dheke, S. K. Panda, S. N. Rout, T. Das and M. Kar, *J Alloys Compd*, 2023, **968**, 172251.

61 F. Albertini, F. Canepa, S. Cirafici, E. A. Franceschi, M. Napoletano, A. Paoluzi, L. Pareti and M. Solzi, *J Magn Magn Mater*, 2004, **272–276**, 2111–2112.

62 F. Albertini, A. Paoluzi, L. Pareti, M. Solzi, L. Righi, E. Villa, S. Besseghini and F. Passaretti, *J Appl Phys*, DOI:10.1063/1.2218470.

63 X. Zhou, W. Li, H. P. Kunkel and G. Williams, *J Magn Magn Mater*, 2005, **293**, 854–862.

64 X. Zhou, H. Kunkel, G. Williams, S. Zhang and X. Desheng, *J Magn Magn Mater*, 2006, **305**, 372–376.

65 M. Pasquale, C. P. Sasso, L. H. Lewis, L. Giudici, T. Lograsso and D. Schlagel, *Phys Rev B Condens Matter Mater Phys*, 2005, **72**, 1–5.

66 X. Zhou, W. Li, H. P. Kunkel, G. Williams and S. Zhang, *J Appl Phys*, DOI:10.1063/1.1853891.

67 Z. Li, H. Yang, K. Xu, Y. Zhang, D. Zheng and C. Jing, *Mater Chem Phys*, 2016, **180**, 156–160.

68 M. Qian, X. Zhang, L. Wei, P. Martin, J. Sun, L. Geng, T. B. Scott and H. X. Peng, *Sci Rep*, 2018, **8**, 2–9.

69 Z. Mo, Q. Liu, W. Hao, L. Li, H. Xie, Q. Fu, X. Gao and J. Shen, *Materials Today Physics*, DOI:10.1016/j.mtphys.2024.101351.

70 E. Palacios, R. Sáez-Puche, J. Romero, Y. Doi, Y. Hinatsu and M. Evangelisti, *J Alloys Compd*, DOI:10.1016/j.jallcom.2021.161847.

71 P. Lampen-Kelley, R. Madhogaria, N. S. Bingham, M. H. Phan, P. M. S. Monteiro, N. J. Steinke, A. Ionescu, C. H. W. Barnes and H. Srikanth, *Phys Rev Mater*, DOI:10.1103/PhysRevMaterials.5.094404.

72 F. Guillou, A. K. Pathak, D. Paudyal, Y. Mudryk, F. Wilhelm, A. Rogalev and V. K. Pecharsky, *Nat Commun*, DOI:10.1038/s41467-018-05268-4.

73 S. Mellari, *International Journal of Air-Conditioning and Refrigeration*, DOI:10.1007/s44189-023-00021-z.

74 R. K. Barik, S. Mishra, M. Khazaei, S. Wang, Y. Liang, Y. Sun, A. Ranjbar, T. L. Tan, J. Wang, S. Yunoki, K. Ohno, Y. Kawazoe and A. K. Singh, *Nano Lett*, DOI:10.1021/acs.nanolett.4c03252.

75 S. Mishra, N. Maity and A. K. Singh, *Phys Rev B*, DOI:10.1103/PhysRevB.110.125406.

76 N. Tiwari, S. Mishra, A. Srivastava, S. Sarkar, V. Chaudhary, M. Paliwal, A. K. Singh and C. S. Tiwary, *Adv Eng Mater*, DOI:10.1002/adem.202401601.

77 K. Ahn, *Elsevier Ltd*, 2024, preprint, DOI: 10.1016/j.jallcom.2023.173378.